ELSEVIER

Materials Science and Engineering B 149 (2008) 270–274

MATERIALS SCIENCE & ENGINEERING B

www.elsevier.com/locate/mseb

Intracavity near-field optical imaging of a mid-infrared quantum cascade laser mode

Paul-Arthur Lemoine [a,1], Virginie Moreau [b,1], Michael Bahriz [b], Yannick De Wilde [a], Raffaele Colombelli [b,*], Luke R. Wilson [c], Andrey B. Krysa [d]

[a] *Laboratoire d'Optique Physique, CNRS-UPR A0005, ESPCI, 75005 Paris, France*
[b] *Institut d'Electronique Fondamentale, Université Paris Sud, CNRS, 91405 Orsay, France*
[c] *Department of Physics and Astronomy, University of Sheffield, Sheffield, UK*
[d] *EPSRC National Centre for III-V Technologies, Department of Electronic & Electrical Engineering, University of Sheffield, Sheffield, UK*

Received 2 August 2007; accepted 29 September 2007

Abstract

We report the direct imaging of Fabry–Pérot standing waves inside the cavity of a mid-infrared quantum cascade laser *via* apertureless scanning near-field optical microscopy. The quantum cascade devices employed present an evanescent wave at the top surface, whose magnitude is directly proportional to the cavity mode intensity in the device core region. Apertureless scanning near-field optical microscopy measurements provide experimental results about the nature of this evanescent field in good agreement with calculations (effective index and electric field decay length).

Keywords: SNOM; Near-field microscopy; Semiconductor lasers; Quantum cascade lasers; Evanescent fields

1. Introduction

In less than three decades, the scanning near-field optical microscope [1] (SNOM) has become an important instrument to probe the optical properties of devices and materials. It allows now one to perform imaging with a resolution well beyond the diffraction limit [1]. The SNOM has been successfully applied at visible [2], infrared [3], terahertz [4], and gigahertz [5] frequencies, producing optical images with a resolution which is sometimes as high as a few hundredths of the observation wavelength. Such resolution offers the possibility to probe the material optical properties far beyond what is achievable with classical far-field microscopy. SNOM microscopy measures the spatial distribution of electromagnetic fields at the surface of a sample. It has been extensively used to study and characterize localized or propagating [6,7] surface plasmons or surface phonon polaritons [8]. SNOMs have also been used to perform spatially resolved studies of absorption [9], Raman scattering [10,11], luminescence [12] or fluorescence [13] on a nanoscopic scale and to characterize passive or active devices [14,15].

In this paper, we report a study using scanning near-field optical microscopy on a mid-IR quantum cascade (QC) laser in operation [16–18]. The QC laser is a semiconductor laser which employs electrical injection. Stimulated light emission results from intersubband transitions in the semiconductor heterostructure which forms the active region of the laser. Thanks to electronic band engineering, QC lasers now can cover the spectral range of mid-IR ($2.9\,\mu m < \lambda < 24\,\mu m$) and THz ($60\,\mu m < \lambda < 200\,\mu m$). Such devices are already used as infrared sources to detect species of chemical and/or biological interest *via* their fingerprint absorptions in the mid-IR [19].

The QC lasers implemented for this study feature an optical mode which leaks evanescently on the top surface [20–22]. For this reason, they are referred hereafter as air-confinement QC lasers. They behave as generators of intense evanescent electric fields whose intensity is electrically controlled [18]. In addition, metallic nanostructures could be deposited on the device top surface for plasmonic applications, meant for instance to launch surface plasmons in a plasmonic circuit. These potential applications motivate the study and the accurate characterisation of

* Corresponding author. Tel.: +33 169157865; fax: +33 169154115.
E-mail addresses: dewilde@optique.espci.fr (Y. De Wilde), colombel@ief.u-psud.fr (R. Colombelli).
[1] These authors contributed equally to this work.

0921-5107/$ – see front matter © 2007 Elsevier B.V. All rights reserved.
doi:10.1016/j.mseb.2007.09.089

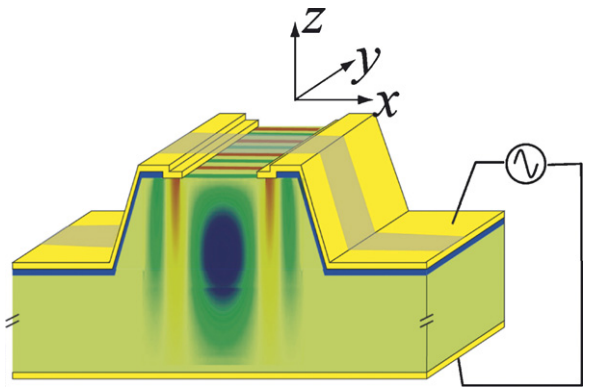

Fig. 1. Scheme of an air-confinement quantum cascade laser. The 2D optical mode ($|E_z|$) is obtained by 2D finite element simulations. The scanning zone is represented in grey. The laser emits from the facets, obtained by cleaving the semiconductor chip. An evanescent electric field is expected to appear on the device top surface.

the optical near-field produced at the surface of air-confinement QC lasers.

2. Device fabrication

The semiconductor growth was performed by metal-organic vapor phase epitaxy (MOVPE). Details of the structure are reported in Ref. [18] and references therein. No semiconductor top claddings were grown, so the mode guiding can be achieved either with a metallic layer (surface–plasmon guiding), or by air-claddings. In this work, the lasers used a Fabry–Pérot ridge resonator with two lateral metallic top contacts for the current injection. Fig. 1 represents the geometry of the devices, on which the result of a 2D finite elements calculation of the optical mode is superimposed. In order to achieve optical guiding, the active region of the QC laser exhibits an interface with air at the device top surface between the top contacts. When the laser is in operation, most of the electromagnetic field inside the cavity is confined in the active region core. Yet, part of it leaks evanescently into the air-claddings above the device and between the metallic top electrodes. The Fabry–Pérot cavity geometry induces the presence of standing waves inside the resonator. The lateral spatial distribution of the evanescent field at the air/active region interface is expected to be the same as that of the standing waves inside the active region. These devices are studied in more details in Ref. [22].

The devices operate at room temperature under pulsed excitation and emit at a wavelength $\lambda \approx 7.7\ \mu m$. The laser ridge widths vary from 26 to 41 μm. The central region on each ridge where the active region is directly in contact with air is typically 10 μm narrower than the ridge itself.

3. Infrared apertureless SNOM: experimental set-up

The development of high transmission optical fibers in the mid-IR spectral range is still in its infancy, and their use in optical fiber SNOMs to map the near-field at wavelengths beyond 5 μm have been so far limited to a few attempts [23]. Apertureless SNOM (aSNOM) based on the scattering of the near-field by the tip apex of an atomic force microscope (AFM) does not require any optical guiding through a fiber. Hence, this technique has proven its ability to map mid-IR near-fields with a resolution as high as 10 nm [3]. For this study, we used a home made aSNOM, employing a quartz tuning fork, which can be operated across a very large range of the optical spectrum, from visible to infrared frequencies [24].

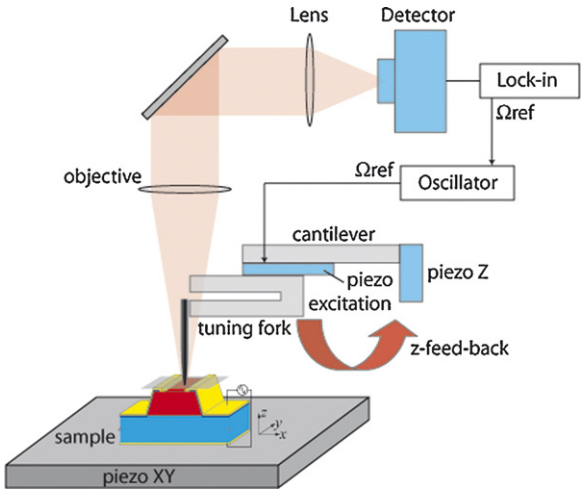

Fig. 2. Schematic view of the experimental set-up. The tungsten tip is mounted at the extremity of the tine of a quartz tuning fork. The piezoceramic plate is controlled with an ac voltage at frequency Ω_{ref} from an oscillator, which produces the mechanical excitation of the tuning fork; this induces a sinusoidal oscillation of the tip at the same frequency. Measuring the voltage on the tuning fork electrodes with a lock-in amplifier allows one to determine the tip oscillation amplitude. A feedback on the piezo Z maintains it at a preset value. Recording the feedback voltage during the lateral scans of the sample under the tip results in a topographic image of scanned area. During its oscillatory movement, the tip apex periodically scatters the evanescent field at the QC laser top surface. A microscope objective collects the scattered field modulated at Ω_{ref}, which is then focused on an HgCdTe infrared detector. The aSNOM signal is obtained by demodulating the signal from the infrared detector at frequency Ω_{ref}. Thus, the aSNOM allows one to record simultaneously a near-field mid-infrared image and a topographical image of the scanned area of the device. The scanned area is represented in grey on the figure.

Our aSNOM is coupled with an AFM whose tip oscillates orthogonally to the sample surface in *tapping-mode*. The tip is made of electrochemically etched 50-μm-diameter tungsten wire placed at the extremity of one arm of a quartz tuning fork. In turn, the tuning fork is glued sideways on a piezoceramic plate, as schematically depicted in Fig. 2. The piezoceramic plate is fed with a sinusoidal voltage at fixed frequency Ω in order to excite a mechanical resonance of the tuning fork. The amplitude of the oscillatory movement of the tip above the surface is monitored *via* the ac voltage on the tuning fork electrodes using a lock-in amplifier. The tip taps periodically onto the sample surface. An electronic feedback is implemented on the piezoelectric stage which controls the average height of the tip above the surface, in order to maintain the oscillation amplitude at a preset value. Thus, by measuring the feedback voltage while scanning the sample under the tip we are able to record the surface topography.

When an electromagnetic field is present at the surface, the tip scatters periodically the near-field at a frequency Ω. The scattered field is collected by a large numerical aperture infrared

microscope objective before being focused onto an HgCdTe liquid nitrogen cooled optical detector. In most experiments, the field, which is scattered by the tip apex, is superimposed on an important far-field background. The use of the tapping-mode enables one to reject the background by demodulating the output signal of the infrared detector at frequencies Ω or at higher harmonics (2Ω, 3Ω, ...) with a lock-in amplifier [25–27]. The signal from the lock-in amplifier as a function of the tip position during the scans produces the near-field optical image of the scanned area, which is acquired simultaneously to the surface topography.

The aSNOM permits to record optical images with a resolution which is roughly given by the radius of curvature of the tip apex, regardless of the wavelength of the scattered field. The tungsten tips used in our aSNOM generally yield a lateral optical resolution ranging between 30 and 100 nm in the near-field images, with a slight improvement when demodulating the optical signal at higher harmonics [28]. Hence, in the mid-IR, a resolution which is two orders of magnitude beyond the diffraction limit is routinely achieved. The near-field scattered by the tip of the aSNOM at the surface of a sample is generally produced by a laser source. Note that a thermal radiation scanning tunnelling microscope (TRSTM) has also recently been developed. This result demonstrated that it is also possible to operate an infrared aSNOM without any external source by detecting the thermal radiation produced by the sample in the near-field [29].

4. Near-field imaging and measurement of the index dispersion

The aSNOM measurements have been performed on several mid-IR air-confinement QC lasers in operation to detect the evanescent field at their top surface. The orientation of the aSNOM tip with respect to the QC laser ridge and the scanned area are sketched in Fig. 2. A portion of the laser mode ($\approx$0.9% in $|E_z|^2$) is expected to leak evanescently into the air claddings above the top surface of the device. The optical arrangement for the detection of the near-field scattered by the tip apex shown in Fig. 2 is thus equivalent to that obtained in dark field microscopy, i.e. there is no far-field background contribution on the detector. This situation is very different from what is done in most aSNOM experiments, which generally employ an external laser illumination of the tip-sample region with propagating waves, resulting in an important far-field background which interferes with the field scattered by the tip on the detector [25–27].

The results presented hereafter have been obtained on a 41 μm-wide air-confinement QC laser ridge. The intensity of the light emitted from the facet of the QC laser as a function of the injected current was initially measured in order to determine the threshold current beyond which laser emission is observed at room temperature. The same type of measurement was then performed by placing the tip at the centre of the laser top surface and by measuring the intensity of the near-field scattered by the tip as a function of the injected current. The threshold current beyond which the near-field signal is non-zero was found to be the same as that observed for far-field laser emission. This indicates that the detected near-field signal is clearly correlated to the onset of lasing inside the semiconductor chip.

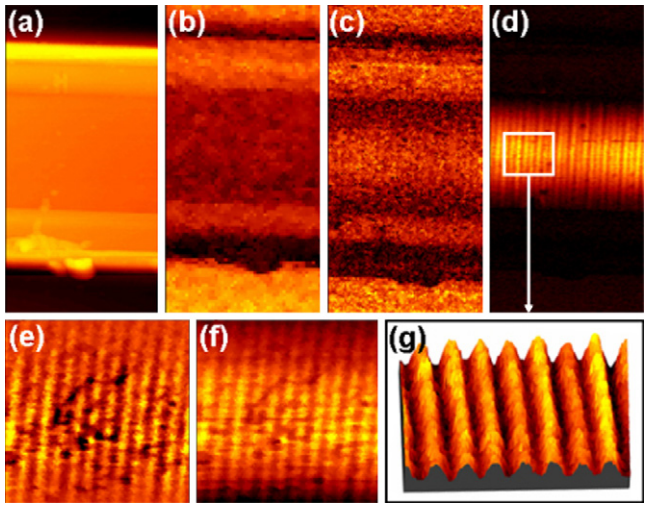

Fig. 3. (a) Topography (AFM) image of the top region of the QC laser investigated in near-field optical microscopy. The scanning range is 30 μm × 60 μm for panels (a)–(d). (b) aSNOM image below laser threshold: only the thermal radiation is detected. (c) Same near-field measurement realized at threshold: the standing waves start to emerge above the active region of the QC laser. (d) Same measurement well above threshold: the standing waves are clearly observable. (e) 15 μm × 15 μm near-field image of the surface of the active region. (f) Same image realized simultaneously by demodulating the detected signal at the laser excitation frequency ≈84 kHz. (g) High resolution 3D view of the standing wave pattern measured well above the laser threshold extracted from image (d). The standing wave interfringe is found to be ≈1.25 μm.

By scanning the device under the tungsten tip across a *xy* plane, we were able to map the field intensity distribution above the top surface. The results of these measurements are presented in Fig. 3. Three operating regimes can be distinguished. The first one is the *thermal regime* which occurs for injected current below laser threshold (see Fig. 3b). In this case, the near-field signal is zero above the active region and dominated by infrared thermal radiation on the metal electrodes, as previously reported in TRSTM measurements in Ref. [29]. At threshold, the *intermediate regime* appears. Near-field thermal radiation is still observable but the evanescent field originating from the laser emission starts to be visible onto the exposed semiconductor surface (see Fig. 3c). A further increase of the injected current allows one to reach the *laser regime*. In this case, the near-field signal associated to the laser mode, which leaks evanescently into the air-claddings, dominates the near-field thermal emission by a few orders of magnitude (see Fig. 3d).

The same kind of results was obtained with air-confinement QC lasers with ridges having different lengths and widths, and also on QC lasers which emit at a different wavelength ($\lambda \approx 9$ μm). Frequency Ω, 2Ω and 3Ω demodulations of the optical signal at the detector were performed and resulted in qualitatively similar images. In the laser regime, images exhibiting the same features were also obtained when demodulating the optical signal at the laser modulation frequency (Fig. 3f). This can be explained by the fact that the field at the laser top surface is purely evanescent, producing dark-field illumination of the tip. Only the near-field scattered by the tip contributes to the optical

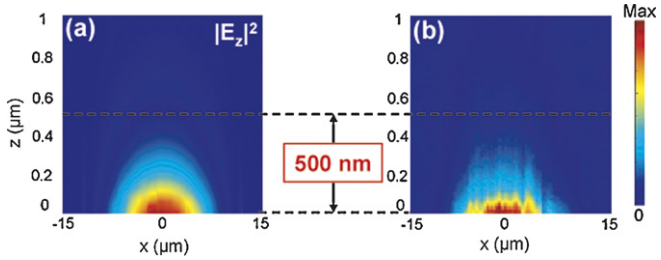

Fig. 4. (a) 2D simulation of the z-component of the evanescent field present at the top surface of the device. (b) Infrared aSNOM image of the intensity measured in a plane xz above the QCL surface. Theory and experiment are in good agreement.

signal on the infrared detector, without any far-field background contribution. There is thus no need to demodulate the optical signal at the tip oscillation frequency or a higher harmonic to extract the near-field image, as it is generally done in aSNOM experiments involving an external laser illumination [25–27].

A close up on the active region area (see Fig. 3g) allows a clear observation of the interference fringes in the near-field optical images. The standing wave pattern results from the interference of counter propagating waves in opposite directions between the two parallel mirror facets of the QC laser, which define a Fabry–Pérot cavity. The distance between subsequent fringes observed in the near-field images is about 1.25 μm. The field intensity in the QCL cavity is expected to be spatially modulated along the cavity axis with a periodicity $p = (\lambda/2n_{\text{eff}})$, which yield an estimate of the effective index of the QCL active region $n_{\text{eff}} \approx 3.1$. On the other hand, the frequency difference between subsequent laser modes observed in the emission spectrum of the device [18] enables one to determine the group index $n_g \sim 3.4$ (if the Fabry-Pérot resonator length is known). The following formula:

$$n_g = n + \lambda \frac{\partial n}{\partial \lambda}$$

allows one to infer the index dispersion. We obtain a value of $\partial n/\partial\lambda \approx -0.037\,\mu\text{m}^{-1}$, in reasonable agreement with simulations obtained within a 2D finite elements approach.

5. Electric field extinction length

Fig. 4(a) shows a two-dimensional simulation of the field magnitude ($|E_z|^2$) in the air-cladding region above the ridge of an air-confinement QC laser in a plane perpendicular to the top surface. Simulations show that the field is evanescent in the z-direction and laterally confined in the x-direction (see Fig. 2 for x, z definitions). The extinction length of the evanescent field in the direction normal to the surface estimated from this simulation is ≈500 nm.

Approach curves in which the aSNOM signal is recorded as a function of the tip-sample separation [18,26] has been performed at equidistant points located along a line perpendicular to the main axis of the ridge on the top surface. These measurements allow one to map the scattered near-field intensity in a plane perpendicular to the ridge surface (xz plane). The results are presented in Fig. 4(b), and they are in good agreement with the 2D simulations (Fig. 4(a)). The decay length of the aSNOM signal at the centre of the structure, as estimated from the approach curves, is found to be 500 nm, which correctly matches the 2D simulations.

6. Conclusion

In conclusion, we have shown that aSNOM measurements of the evanescent field present above the air/active-region interface of mid-IR air-confinement QC lasers produce images of standing waves due to spatial confinement inside the laser cavity. aSNOM provides an exhaustive characterization technique of the lateral and vertical field distribution for such QC laser devices. Future experiments will focus on imaging the propagation of surface plasmons above the surface of patterned metal structures QC lasers at infrared frequencies.

Acknowledgements

The authors thank O. Painter, R. Perahia F. Julien, and C. Sirtori for useful discussions. One of the authors (P.-A.L.) acknowledges the Délégation Générale de l'Armement for financial support. This work was conducted as part of a EURYI scheme award (see www.esf.org/euryi).

References

[1] D.W. Pohl, et al., Appl. Phys. Lett. 44 (1984) 651–653.
[2] F. Zenhausern, Y. Martin, H.K. Wickramasinghe, Science 269 (1995) 1083–1085.
[3] A. Lahrech, R. Bachelot, P. Gleyzes, A.C. Boccara, Opt. Lett. 21 (1996) 1315–1317.
[4] H.T. Chen, R. Kersting, G.C. Cho, Appl. Phys. Lett. 83 (2003) 309–311.
[5] B. Knoll, F. Keilmann, A. Kramer, R. Guckenberger, Appl. Phys. Lett. 70 (1997) 2667–2669.
[6] S. Grésillon, L. Aigouy, A.C. Boccara, J.C. Rivoal, X. Quelin, C. Desmarest, P. Gadenne, V.A. Shubin, A.K. Sarychev, V.M. Shalaev, Phys. Rev. Lett. 82 (1999) 4520–4523.
[7] L. William, Barnes1, Alain Dereux, W. Thomas, Ebbesen, Nature 424 (2003) 824.
[8] A. Huber, N. Ocelic, D. Kazantsev, R. Hillenbrand, Appl. Phys. Lett. 87 (2005) 081103.
[9] B. Knoll, F. Keilmann, Nature 399 (1999) 134–137.
[10] A. Hartschuh, E.J. Sanchez, X.S. Xie, L. Novotny, Phys. Rev. Lett. 90 (2003) 95503.
[11] N. Hayazawa, Y. Inouye, Z. Sekkat, S. Kawata, J. Chem. Phys. 117 (2002) 1296–1301.
[12] F. Intonti, V. Emiliani, Ch. Lienau, T. Elsaesser, V. Savona, E. Runge, R. Zimmermann, R. Nötzel, K.H. Ploog, Phys. Rev. Lett. 87 (2001) 076801.
[13] J. Erik, Sánchez, X. Lukas Novotny, Sunney Xie, Phys. Rev. Lett. 82 (1999) 4014–4017.
[14] F. Chen, A. Itagi, J.A. Bain, D.D. Stancil, T.E. Schlesinger, L. Stebounova, G.C. Walker, B.B. Akhremitchev, Appl. Phys. Lett. 83 (2003) 3245.
[15] E. Cubukcu, E.A. Kort, K.B. Crozier, F. Capasso, Appl. Phys. Lett. 89 (2006) 093120.
[16] J. Faist, F. Capasso, D.L. Sivco, C. Sirtori, A.L. Hutchinson, A.Y. Cho, Science 264 (1994) 553.
[17] C. Gmachl, F. Capasso, D.L. Sivco, A.Y. Cho, Rep. Prog. Phys. 64 (2001) 1553.
[18] V. Moreau, P.A. Lemoine, M. Bahriz, Y. De Wilde, R. Colombelli, L.R. Wilson, A.B. Krysa, Appl. Phys. Lett. 90 (2007) 201114.
[19] F.K. Tittel, Y. Bakhirkin, A.A. Kosterev, G. Wysocki, Rev. Laser Eng. 34 (2006) 275–284.

[20] W. Schrenk, N. Finger, S. Gianordoli, L. Hvozdara, G. Strasser, E. Gornik, Appl. Phys. Lett. 77 (2000) 2086.
[21] D. Hofstetter, T. Aellen, M. Beck, J. Faist, IEEE Photon. Technol. Lett. 12 (2000) 1610.
[22] V. Moreau, M. Bahriz, R. Colombelli, R. Perahia, O. Painter, L.R. Wilson, A. Krysa, Opt. Express 15 (2007) 14861–14869.
[23] D.T. Schaafsma, et al., Opt. Eng. 38 (1999) 1381–1385.
[24] Y. De Wilde, F. Formanek, L. Aigouy, Rev. Sci. Inst. 74 (2003) 3889–3891.
[25] B. Knoll, F. Keilmann, Opt. Comm. 182 (2000) 321–328.
[26] F. Formanek, Y. De Wilde, L. Aigouy, J. Appl. Phys. 93 (2003) 9548–9552.
[27] G. Wurtz, R. Bachelot, P. Royer, Eur. Phys. J. 5 (1999) 269–275.
[28] F. Formanek, Y. De Wilde, L. Aigouy, Y. Chen, Scanning 26 (2004) 63–67.
[29] Y. De Wilde, F. Formanek, R. Carminati, B. Gralak, P.-A. Lemoine, K. Joulain, J.-P. Mulet, Y. Chen, J.-J. Greffet, Nature 444 (2006) 740–744.